

Cite this: *Mater. Adv.*, 2026,  
7, 3722

# *In situ* synchrotron X-ray diffraction studies of the high-temperature hydrogen reduction of New Zealand titanomagnetite ironsand

Morgan Lowther,<sup>id</sup>\*<sup>a</sup> Bridget Ingham,<sup>id</sup><sup>b</sup> Martin J. Ryan,<sup>id</sup>†<sup>b</sup> Sigit Prabowo,<sup>id</sup><sup>a</sup> Mohammad Nusseh,<sup>id</sup><sup>a</sup> Raymond J. Longbottom,<sup>id</sup><sup>c</sup> Bavinesh Maisuria,<sup>id</sup><sup>a</sup> Sarah Spencer,<sup>a</sup> Brian J. Monaghan,<sup>id</sup><sup>c</sup> Mark H. Reid,<sup>id</sup><sup>d</sup> and Chris W. Bumby<sup>id</sup><sup>a</sup>

To characterise the hydrogen fluidised bed reduction of New Zealand titanomagnetite ironsand, this study reports the hydrogen reduction behaviour *in situ* via synchrotron X-ray diffraction at 938 °C. Titanomagnetite is directly compared with a synthetic magnetite. The crystalline phase evolution and changes in lattice parameter confirm that Ti significantly alters the reduction pathway at high temperature, following a 5-stage reduction process. Stabilisation of  $\text{Fe}_{(3-x)}\text{Ti}_x\text{O}_4$  (inverse spinel) by Ti results in two distinct reduction pathways that favour reduction of low Ti content crystallites. First, reduction of inverse spinel *via* wüstite results in the exsolution of an amorphous Ti rich oxide phase. This reaction halts as FeO is metallised, causing a plateau in the net lattice parameter of  $\text{Fe}_{(3-x)}\text{Ti}_x\text{O}_4$ . A transition to the accumulation of Ti during direct reduction of the remaining inverse spinel is followed by conversion to ilmenite and pseudobrookite phases. Lower Ti content inverse spinel reduces first throughout the entire reduction process, emphasising the significant stabilising effect of Ti content.

Received 15th October 2025,  
Accepted 3rd March 2026

DOI: 10.1039/d5ma01165e

rsc.li/materials-advances

## 1. Introduction

Decarbonisation of steelmaking is a key requirement for reducing anthropogenic  $\text{CO}_2$  output, accounting for 8% of global energy system emissions in 2022 and the largest source of greenhouse emissions for a single industrial process.<sup>1,2</sup> Hydrogen direct reduction represents the primary alternative to traditional carbothermic ironmaking processes, with significant potential decrease in emissions as the renewable production of hydrogen increases.<sup>3,4</sup>

Parallel to the need for low emission technology, the decreasing availability of high-grade binary iron oxide ores makes the reduction behaviour of ternary oxides crucial for long-term sustainability.<sup>5</sup> Significant quantities of titanium-iron oxide ores are available globally, with large exemplar deposits in China, Indonesia, India, and New Zealand.<sup>6–10</sup> The concentration and quality of such ore varies by location, with extensive deposits of

very high grade mineral sands occurring on the coast of North Island Aotearoa, New Zealand (NZ).<sup>11,12</sup> The combination of high grade ore, abundant local renewable energy sources, and the global need to decarbonise steelmaking, make the hydrogen reduction of NZ ironsands of particular interest.<sup>13</sup>

These ores consist primarily of two solid solution series. First, the titanomagnetite inverse spinel  $\text{Fe}_{(3-x)}\text{Ti}_x\text{O}_4$  solid solution, ranging from magnetite ( $x = 0$ ) to ulvospinel ( $x = 1$ ). Second, the  $\text{Fe}_{(2-x)}\text{Ti}_x\text{O}_3$  series, between hematite ( $x = 0$ ) and ilmenite ( $x = 1$ ). Alongside acting as a significant source of metallic iron, reduction of titanomagnetite is a necessary first step in the co-production of high value companion metals such as Ti and V.<sup>14</sup> For Fe production, a high Fe content titanomagnetite is preferable, with ilmenite primarily exploited for Ti production.

Unlike the sequential reduction of iron oxides as described by the Bauer-Glaessner diagram, the hydrogen reduction of titanomagnetite ores follows a complex multi-phase pathway that is highly temperature and composition dependent. Previous studies have established the importance of Ti content in determining this behaviour. High Ti ores ( $\text{Ti}/(\text{Ti} + \text{Fe}) > 20\%$ ) progress directly from inverse spinel to ilmenite formation across a wide temperature range.<sup>15</sup> At lower Ti content, however, varying reduction pathways have been observed in the 700–1000 °C range.<sup>16</sup> Understanding the order in which phases form and the distribution of Ti is crucial for optimisation of the reduction process. This is particularly the case when reducing

<sup>a</sup> Robinson Research Institute, Victoria University of Wellington, P. O. Box 33436, Lower Hutt 5046, New Zealand<sup>b</sup> Callaghan Innovation, P. O. Box 31310, Lower Hutt 5040, New Zealand<sup>c</sup> Pyrometallurgical Research Group, Faculty of Engineering and Information Sciences, University of Wollongong, Wollongong, NSW 2522, Australia<sup>d</sup> Australian Centre for Neutron Scattering, Australian Nuclear Science and Technology Organisation, Sydney, NSW, Australia

† Martin Ryan is acknowledged posthumously as a significant contributor to this work.



particulate ores in a fluidised bed, in which the migration of Ti plays a major role in regulating sticking.<sup>17</sup>

Alongside Ti and Fe, titanomagnetite ores often contain other contaminant elements such as Al, Mg, and lower concentration substituents such as V and Mn. Both Mg and Al are able to substitute for Fe throughout the matrices of magnetite and hematite, forming equivalent solid solutions to the  $\text{Fe}_{(2-x)}\text{Ti}_x\text{O}_3$  and  $\text{Fe}_{(3-x)}\text{Ti}_x\text{O}_4$  phases.<sup>18–21</sup> Microstructural studies of iron-sand reduction indicate that Al is strongly co-located with Ti throughout the reduction process, whilst Mg is more evenly dispersed within Fe bearing phases.<sup>16,22,23</sup>

Temperature dependent miscibility gaps and phase instabilities within the Fe–Ti–O ternary further complicates predicting the reduction pathway at elevated temperature. The ferropseudobrookite solid solution ( $\text{Fe}_x\text{Ti}_{(3-x)}\text{O}_5$ ,  $1 \leq x \leq 2$ ) is stabilised at high temperature, but has unstable regions in the temperature range of 600–1150 °C.<sup>24</sup> Further, miscibility gaps in the inverse spinel  $\text{Fe}_{(3-x)}\text{Ti}_x\text{O}_4$  and hematite-ilmenite  $\text{Fe}_{(2-x)}\text{Ti}_x\text{O}_3$  series occur below 550 °C and 800 °C respectively.<sup>25,26</sup>

Quantitative *in situ* monitoring of crystallographic phases is required to understand reaction pathways. Here we report *in situ* powder diffraction measurements of the high temperature hydrogen reduction of both mineral titanomagnetite and synthetic magnetite using high-resolution synchrotron X-rays. This technique allows us to not only track the major phases which evolve during the reaction, but also offers additional insight into materials parameters such as crystallite size, strain, and other structural variations. Coupled with sampling of partially reduced material from a fluidised bed reactor under equivalent conditions, microstructural changes can be correlated with the in-depth *in situ* crystallographic data.

Results show that the presence of Ti within the magnetite lattice has a significant effect on the reduction pathway, increasing the number of intermediate phases to achieve complete metallisation. As the titanium content of inverse spinel increases, production of wüstite becomes unfavourable. This results in a switch in the reduction pathway to direct metallisation of the inverse spinel, and the exsolution of Ti.

## 2. Experimental method

### 2.1. Materials

Titanomagnetite ironsand was sourced as an unmilled mineral concentrate (Waikato North Head, New Zealand), with a synthetic magnetite (Höganäs) used as a comparator. These samples are referred to as ‘TTM’ and ‘MAG’ respectively. Elemental analysis was performed by X-ray fluorescence (XRF) (Shimadzu EDX-7200), with results given in Table 1.

### 2.2. Fluidised bed experiments

The hydrogen reduction behaviour of TTM was investigated using isothermal fluidised bed experiments. A simplified schematic of the fluidised bed reactor and sampling system is shown in Fig. 1. Further details of the experimental apparatus can be found in previously published literature.<sup>16,17,27</sup>

Table 1 XRF analysis of titanomagnetite ironsand (TTM) and synthetic magnetite (MAG)

	Mass %		Cation ratio		
	TTM	MAG	TTM	MAG	
Total iron ( $\text{Fe}_T$ )	60.5	69	Fe	80	98.6
$\text{TiO}_2$	8.1	0.3	Ti	7.5	0.3
$\text{Al}_2\text{O}_3$	3.5	0.2	Al	5.1	0.3
$\text{MgO}$	2.6	0.2	Mg	4.8	0.4
$\text{V}_2\text{O}_5$	0.6	0.2	V	0.5	0.2
$\text{MnO}$	0.6	0.05	Mn	0.6	0.1
$\text{CaO}$	0.2	0.03	Ca	0.3	0.04
$\text{P}_2\text{O}_5$	0.1	0.02	P	0.1	0.02
$\text{SiO}_2$	1	0.1	Si	1.2	0.1

Unmilled TTM was sieved to a 90–150  $\mu\text{m}$  size fraction. A bed mass of 100 g was used for each experiment. The reactor was purged with nitrogen gas at an input flow rate of 50  $\text{cm}^3 \text{s}^{-1}$  (3 standard litres per minute) during heating to a bed temperature of 938 °C. Gas flow was then switched to hydrogen at an input flow rate of 83  $\text{cm}^3 \text{s}^{-1}$  (5 standard litres per min) for the duration of the experiment. Samples of approximately 2 g were drawn into a water quenched sample pot at predetermined timepoints during the reduction. In order to acquire samples at timepoints of 1 min and 3 min, the entire bed was quenched with nitrogen.

**2.2.1. Sample characterisation.** The crystalline phases present in fluidised bed samples were analysed by X-ray diffraction under ambient conditions (Rigaku Smartlab 3 kW). Scans were performed using a Co-K $\alpha$  (1.79 Å) source, with step size of 0.02° and collection time of 0.4 s per step.

Additional samples were mounted and polished to cross-section particles for scanning electron microscopy. Backscattered

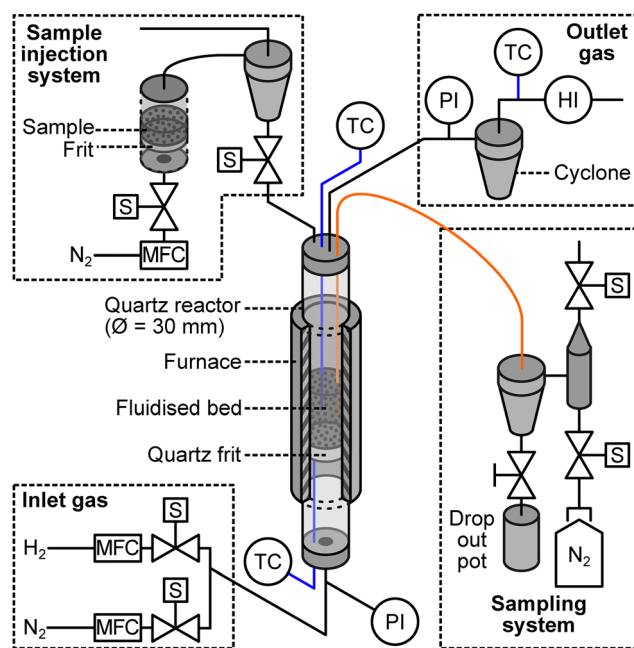


Fig. 1 Schematic of the experimental setup used for fluidised bed reduction. HI: humidity sensor; PI: pressure sensor; TC: thermocouple. Photographs of the reactor assembly are available in Supplementary A.



electron (BSE) images were taken (Hitachi SU7000) of representative particles. Electron dispersive X-ray spectroscopy (EDS) mapping of selected regions was performed (Oxford EDS Ultimex 100, AZtec Version 6.1) to assess the distribution of key elements. Maps are presented as apparent concentration.

### 2.3. Synchrotron experiments

Samples of MAG and TTM were ground to a particle size of 5–10  $\mu\text{m}$  for synchrotron measurements. The ground samples were packed in 0.7 mm diameter quartz capillaries (Charles Supper) and mounted in a gas flow cell on the Powder Diffraction beamline at the Australian Synchrotron, shown in schematic form in Fig. 2. A Cyberstar hot air blower was mounted beneath the capillary and heated to its maximum setpoint temperature of 1000  $^{\circ}\text{C}$ , with a target experimental temperature of approximately 950  $^{\circ}\text{C}$ . The actual temperature at the sample position was measured as 938  $^{\circ}\text{C}$  using a thermocouple and calibrated using the lattice parameter of an *in situ* platinum wire. The hot zone was approximately 2 mm wide; the X-ray beam size at the sample was 1 mm and centred in the middle of the hot zone. The X-ray wavelength was calibrated using a  $\text{LaB}_6$  standard (NIST 660b), and established as 0.5889  $\text{\AA}$  (21.00 keV). Data were collected in a continuous fashion using a Mythen detector spanning 80 $^{\circ}$  of arc in  $2\theta$ . To cover gaps between the detector modules, the detector was rotated back and forth by 0.5 $^{\circ}$  in  $2\theta$  from one measurement to the next. The exposure time for each measurement was 30 s. Data were normalised to the incident beam intensity, merged in time and averaged to a step size of 0.005 $^{\circ}$  in  $2\theta$  according to the method described in Materić *et al.*,<sup>28</sup> which results in no loss of time resolution.

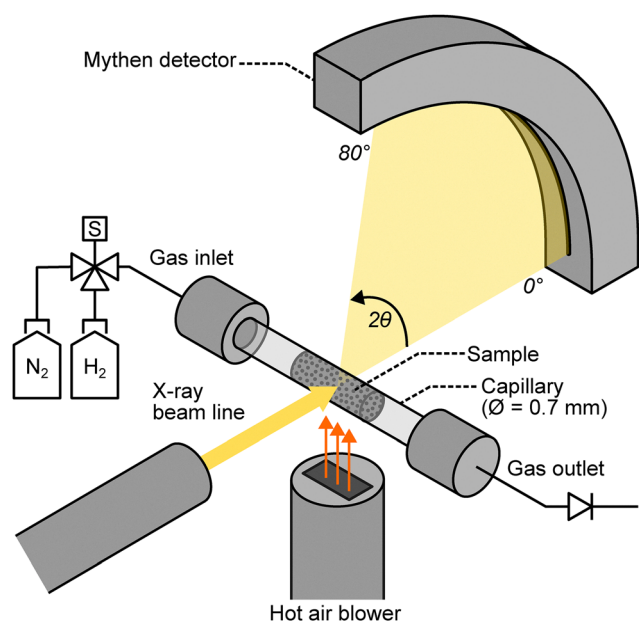


Fig. 2 Schematic of the experimental setup used at ANSTO for synchrotron diffraction measurements of hydrogen reduction at elevated temperature. Photographs of the experimental apparatus are available in Supplementary A.

Experiments were performed under isothermal conditions, with an input gas flow rate of 2.08  $\text{cm}^3 \text{s}^{-1}$  (125 standard cubic centimetres per min), equivalent to approximately 8.3  $\text{cm}^3 \text{s}^{-1}$  at 938  $^{\circ}\text{C}$ . The hot air blower was heated to temperature and moved into place beneath the sample with nitrogen gas flowing through the capillary. Continuous diffraction measurements were begun, and after 10 measurements the gas was remotely switched to hydrogen. The experiment was stopped after 90 minutes or once the sample had fully reacted and reached a steady state, whichever came first. At the conclusion of each experiment, the gas flow was switched back to nitrogen, measurements were stopped, the hot air blower was moved out of position, the inlet and outlet gas valves were closed, and the capillary was removed from the flow cell.

**2.3.1. Data analysis.** Rietveld refinement was performed on the processed synchrotron XRD data using Topas 4.2 (Bruker). The instrument parameters were refined using the  $\text{LaB}_6$  standard, and then fixed for all analyses. Structural models were included for the predominant crystalline Fe and Ti containing phases. Variable parameters included the wt%, lattice parameters, crystallite size (Lorentzian and/or Gaussian), and strain (Lorentzian and/or Gaussian). Temperature factors were constrained to be the same for the same element across all phases, and for oxygen this was fixed to the average value obtained at the start of each experiment. For the experiments on TTM, multiple phases were required to fit the inverse spinel magnetite phase for part of the time. In these cases, each phase was constrained to have the same crystallite size and strain parameters; only the lattice parameters were fitted independently. Details of the structural models used are given in Supplementary B.

The estimated reduction degree (RD) was calculated on a per-cation site basis, calculating the molar ratio of phases present assuming ideal stoichiometry and the resulting weighted average oxidation state of iron. Note that this neglects any compositional changes within phases, and is provided as an indicator of reaction progress and not as a precise instantaneous measure of the degree of reduction.

## 3. Results

### 3.1. Fluidised bed reduction behaviour

**3.1.1. Crystalline phase composition.** In the unreduced state, TTM is predominantly inverse spinel ( $\text{Fe}_{(3-x)}\text{Ti}_x\text{O}_4$ ) with approximately 10% titanohematite ( $\text{Fe}_{(2-x)}\text{Ti}_x\text{O}_3$ ) present. Hematite is rapidly reduced (prior to  $t = 1$  min), with the reduction of the inverse spinel and formation of wüstite ( $\text{Fe}_{(1-x)}\text{O}$ ) also observed prior to this first timepoint (Fig. 3). The formation of metallised Fe becomes apparent after 3 minutes of reduction, at the peak of observed wüstite content of 23%.

Both inverse spinel and wüstite reduce during the remaining reaction, with formation of pseudobrookite observed in the final timepoint ( $t_f = 40$  min). A metallisation degree of  $\sim 90\%$  and calculated reduction degree of 96% is achieved.

**3.1.2. Microstructural analysis.** The microstructural evolution of TTM during fluidised bed hydrogen reduction is shown



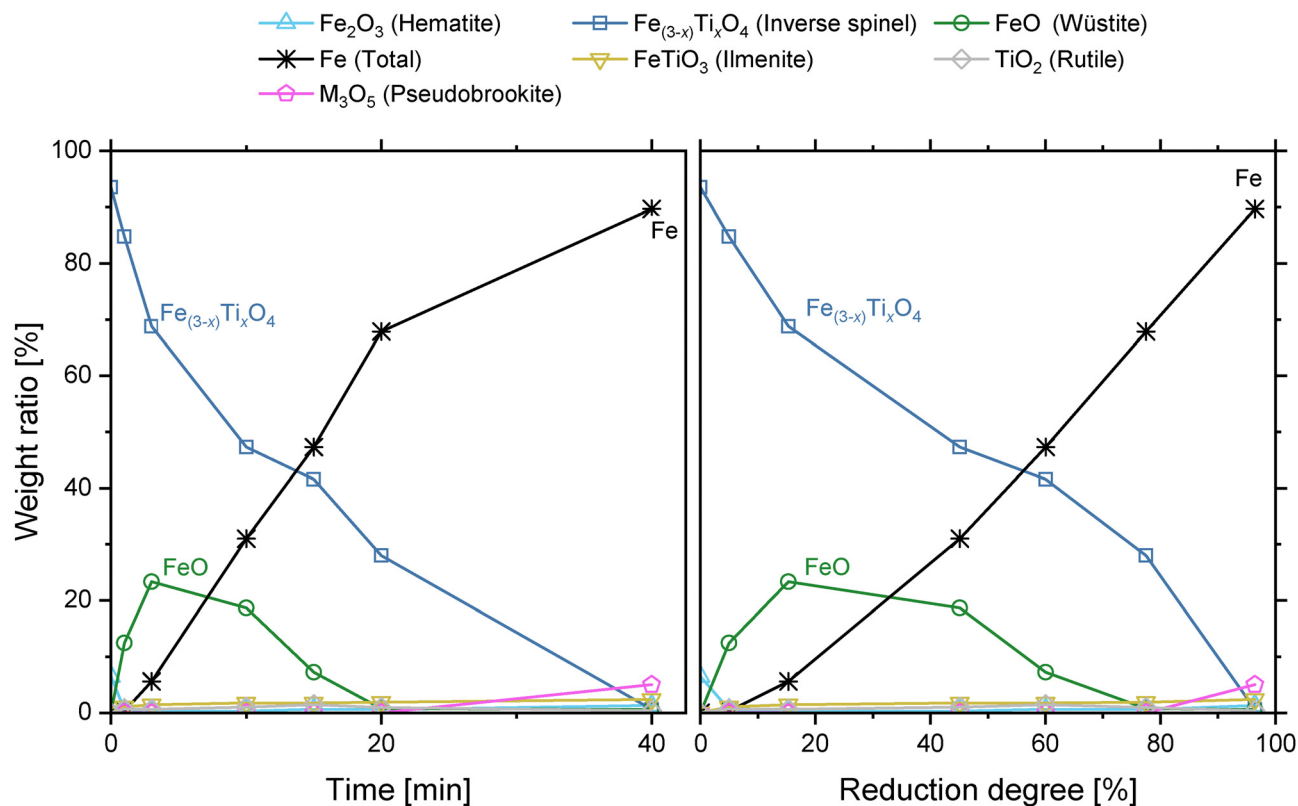


Fig. 3 Crystalline phase composition against time (left) and against estimated degree of reduction (right) for TTM. Samples taken from fluidised bed reduction at 938 °C and measured at room temperature are shown.

in Fig. 4. The homogeneous inverse spinel structure rapidly converts to a latticework of 0.5  $\mu\text{m}$  wide wüstite channels embedded in the spinel matrix. An oxide shell develops and stabilises at 3.5  $\mu\text{m}$  thick over the first 15 minutes. During the reduction of wüstite ( $t > 3$  min), metallic Fe and voids form, correlating with the anticipated  $\sim 28\%$  volume reduction as wüstite metallises. This transformation front progresses from the particle surface to the core as the reduction continues. In the final stages of reduction, iron precipitates at the outer surface of particles (Supplementary C).

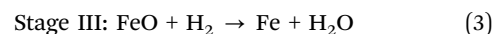
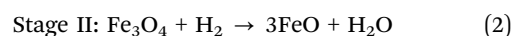
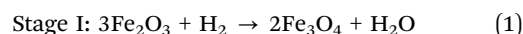
Wüstite is shown to have a lower solubility for Ti than the surrounding inverse spinel matrix with similar behaviour observed for Al (Fig. 5a). As wüstite reduces, the formation of voids and metallised Fe follows the microstructure of prior wüstite channels.

The outer shell consists of a 0.5  $\mu\text{m}$  thick outermost oxide layer enriched in Mg, and an Fe denuded oxide region enriched in Ti and Al (Fig. 5b). A visible correlation of Ti, Al, and O distribution is present within the particle as reduction progresses (Supplementary C). An increase in the volume fraction of Fe within regions where wüstite has already been reduced indicates continued reduction of the remaining inverse spinel. This behaviour correlates with the observed crystalline phase behaviour in synchrotron and XRD analyses. No other segregated Ti enriched phase can be directly observed in these images, excluding the Fe-denuded outer shell.

### 3.2. Synchrotron reduction behaviour

**3.2.1. Crystalline phase composition.** At 938 °C, both TTM and MAG samples are composed predominantly of inverse spinel (Fig. 6). A small amount (approx. 10%) of rhombohedral titanohematite is present in both cases. Note in the experiments using MAG that these phases will approximate the end member compositions of magnetite ( $\text{Fe}_3\text{O}_4$ ) and hematite ( $\text{Fe}_2\text{O}_3$ ) respectively, whilst in TTM that titanium may also be incorporated.

The rapid onset of hematite reduction to inverse spinel indicates the start of reaction of hydrogen gas with the sample at the measurement position ( $t_0 = 0$ ). The MAG sample follows a well-defined stepwise reduction with each reaction reaching the endpoint concurrent with the start of the next reaction:



This three-stage hydrogen reduction pathway is consistent with existing literature.<sup>29,30</sup> The small 5–10  $\mu\text{m}$  particle size will encourage completion of sequential reactions compared to coarser material.

The reduction process observed in TTM is significantly more complex than MAG, with five distinct reduction stages. The



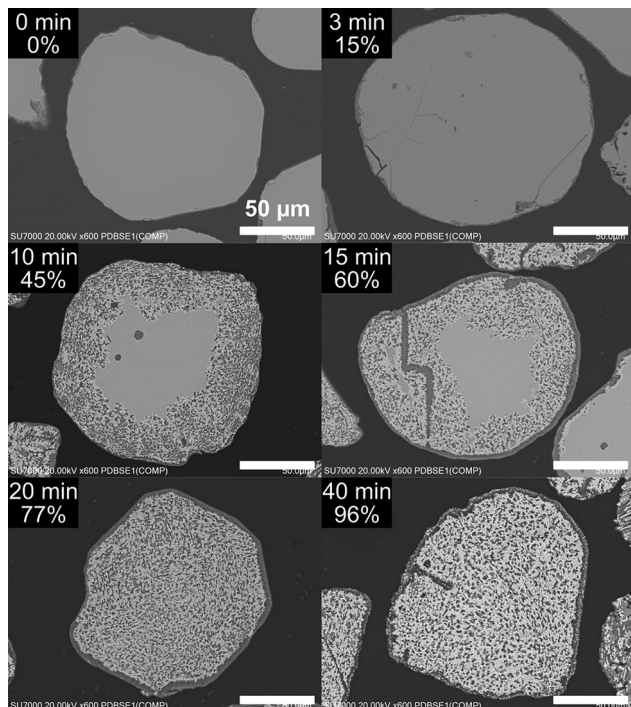
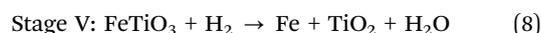
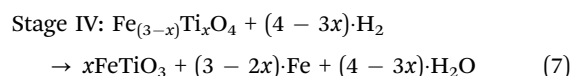
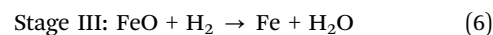
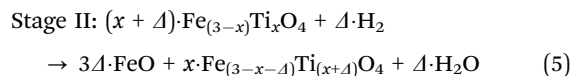
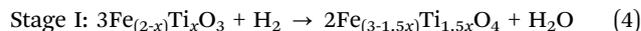


Fig. 4 Backscattered electron micrographs of representative TTM particles sampled from fluidised bed reduction. The time of sampling and estimated degree of reduction is labelled for each image. Microstructural evolution progresses from a homogeneous microstructure through a latticework of wüstite channels, and subsequent conversion of channels to metallic Fe and voids.

approximate boundaries of these stages are demarcated in Fig. 6b. Theoretical reduction equations are as follows, with the  $x$  representing varying degrees of Ti enrichment and  $\Delta$  representing arbitrary hydrogen quantities for a given reaction:



The formation of ilmenite in Stage IV (eqn (7)) has been simplified to assume strict stoichiometry of the product phase. Unlike in MAG, these reactions are not strictly confined to the boundaries of each stage as shown, but are instead the predominant or characteristic reaction during that stage. For example, reduction of wüstite to metallic iron begins prior to the demarcated start of Stage III.

Comparing behaviour to that observed in fluidised bed samples, a good correlation is shown by these data and comparison of synchrotron and *ex situ* XRD patterns (Supplementary E). Synchrotron data is representative of the fluidised bed reduction behaviour.

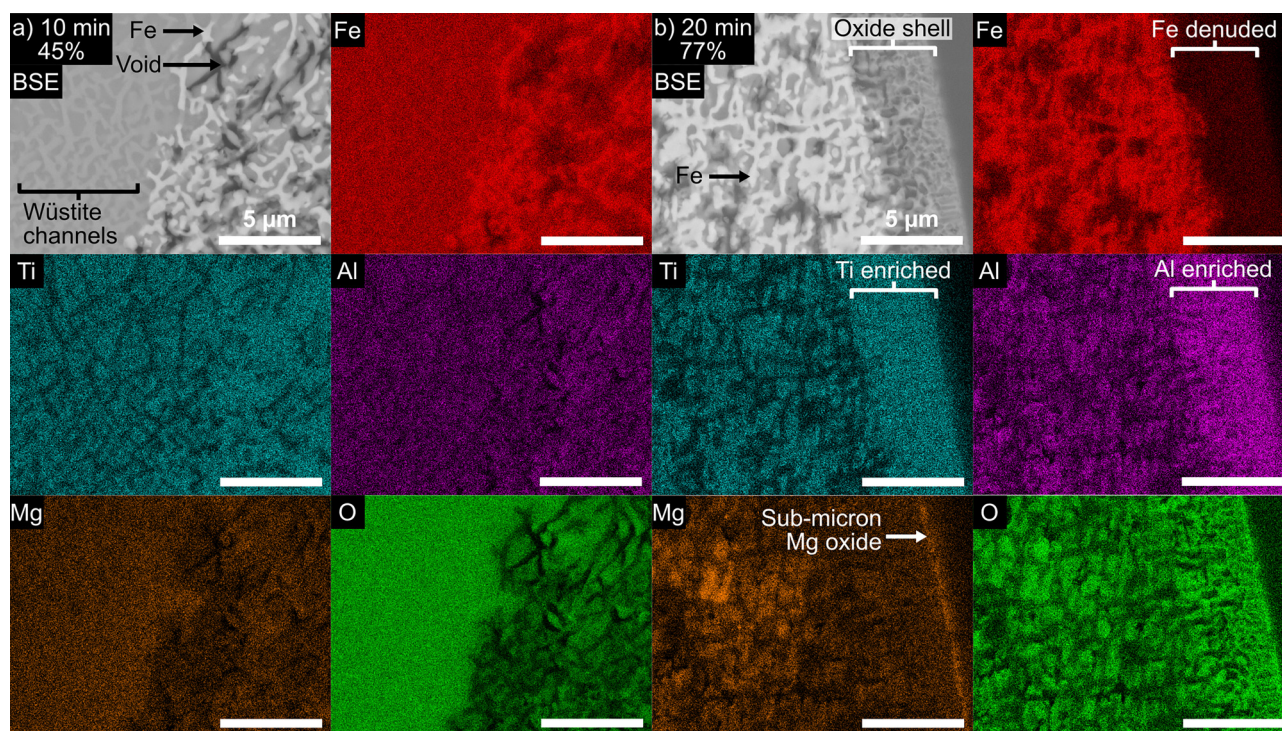


Fig. 5 Backscattered electron micrograph and apparent concentration EDS maps of representative TTM particles sampled from fluidised bed reduction, showing: (a) the interface between wüstite at  $t = 10$  min, RD 45%; and (b) the outer shell at  $t = 20$  min, RD 77%. All scalebars are 5  $\mu\text{m}$ . Further EDS map images at additional timepoints are available in Supplementary B.



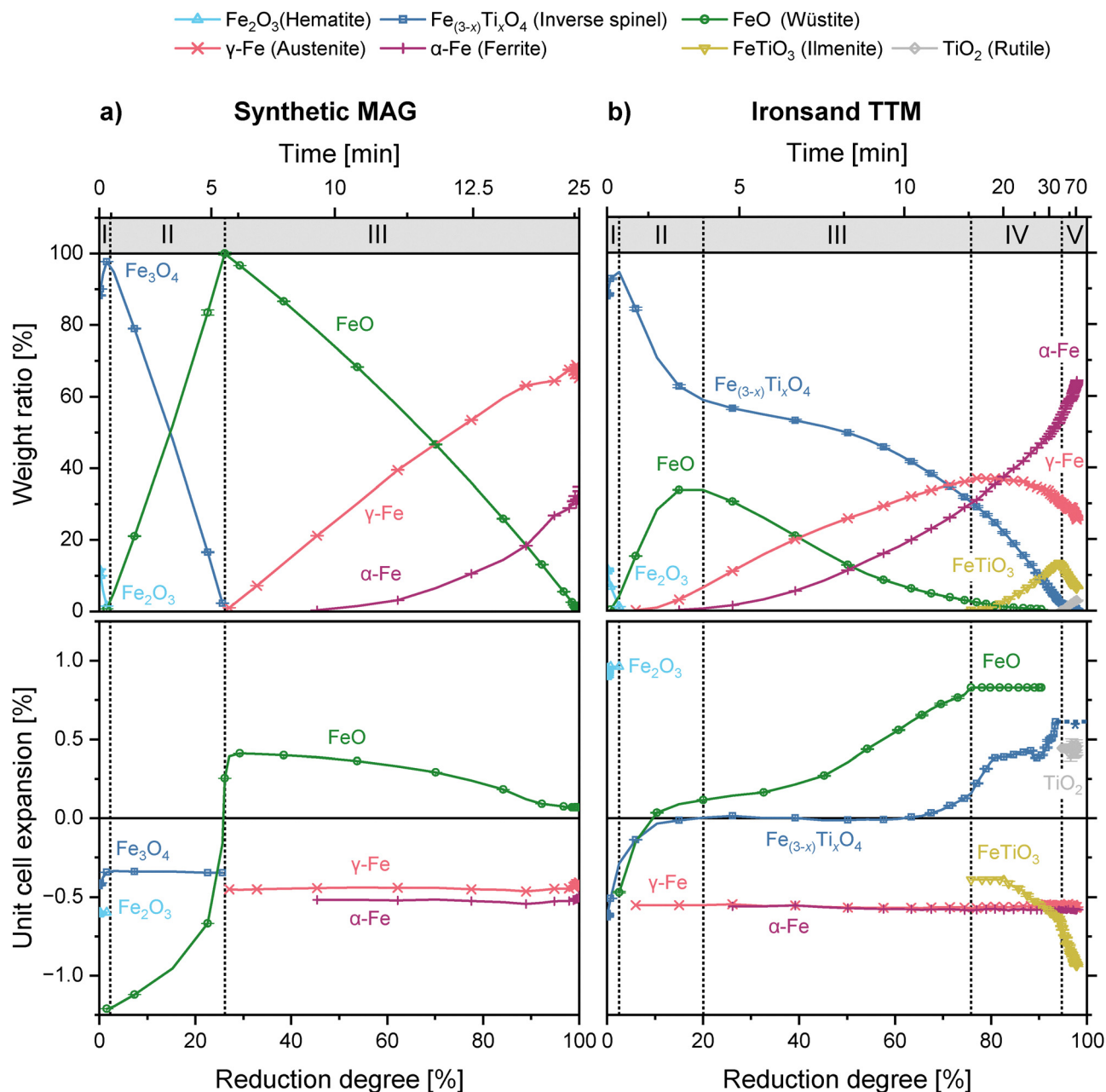


Fig. 6 Crystalline phase composition and relative change in unit cell volume during isothermal hydrogen reduction at 938 °C, for (a) MAG (left) and (b) TTM (right) plotted against time and estimated degree of reduction, calculated assuming ideal stoichiometry. Unit cell expansion is relative to reference data. The average measured unit cell volume of  $\text{Fe}_{(1-x)}\text{O}$  in MAG was used as a reference for wüstite. For improved visual clarity each second timepoint is plotted. The approximate boundaries of reaction stages are labelled. \* dashed line represents region for which accurate fitting of inverse spinel peak was not possible.

**3.2.2. Lattice parameter.** Significant changes are observed in the lattice parameters of the crystallographic phases as reduction progresses, showing distinct changes in behaviour between stages (Fig. 6). Relative lattice volume change is reported to better compare cubic and non-cubic crystal structures. The relative change in unit cell volume is calculated against reference data. A summary of current reference data for the compositional and temperature dependency of lattice parameters for phases in this system is presented in Supplementary D.<sup>18–21,31–44</sup> Due to the strong dependency of lattice parameter

on stoichiometry and oxygen partial pressure for wüstite, the average lattice parameter measured for the MAG sample was used as a reference in this case.<sup>45</sup> Changes in the inverse spinel lattice are most prominent in the TTM sample, and are indicative of partitioning of Ti and other solute atoms throughout the reduction process (Fig. 6b).

The diffraction peaks of the inverse spinel phase in TTM show significant asymmetry once reduction begins. Asymmetric peaks were fitted using the sum of three separate inverse spinel structural models (Fig. 7a), each having different lattice



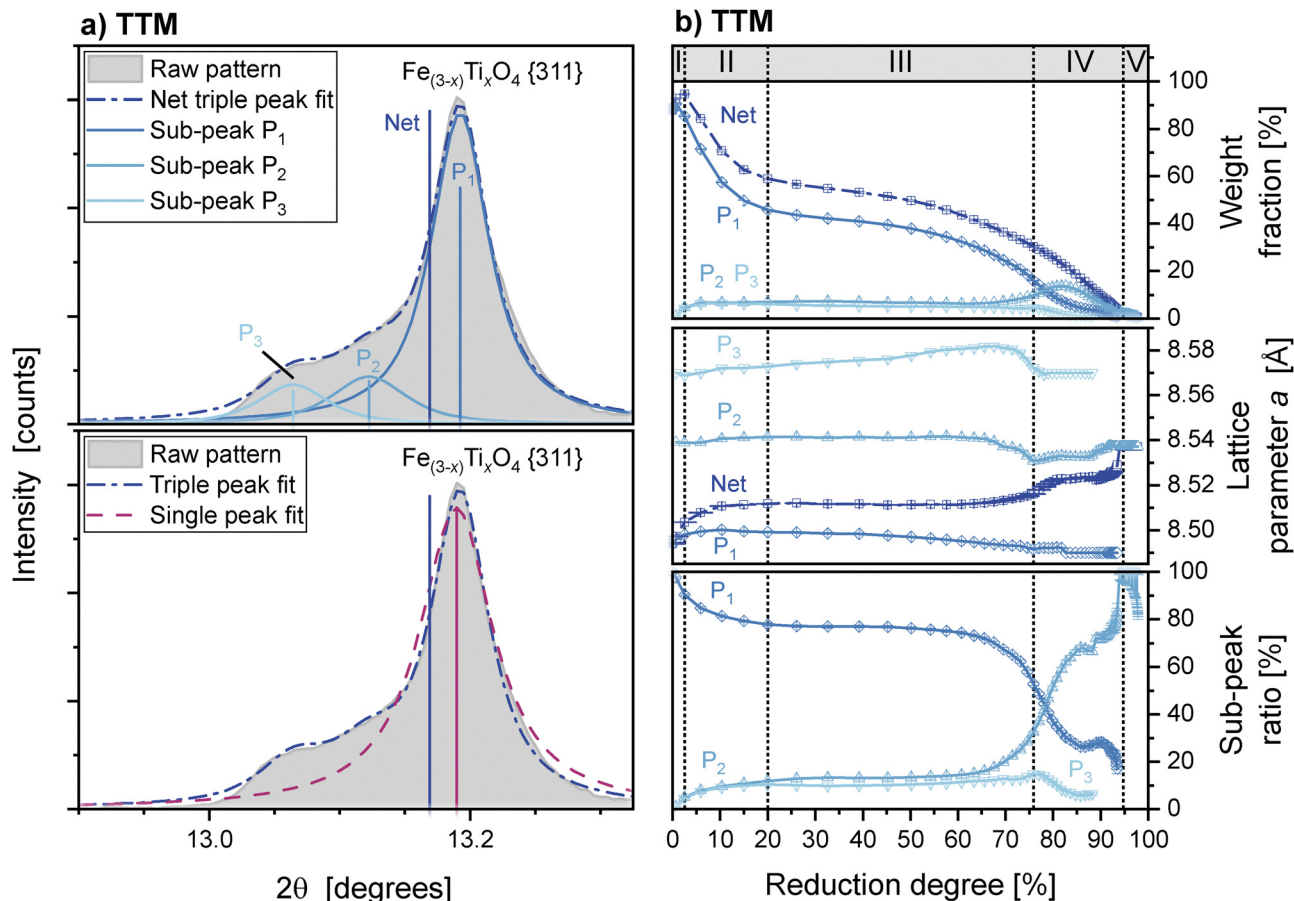


Fig. 7 (a) Example of fitting three separate pseudo-Voigt peaks to an asymmetric inverse spinel peak (top), with comparison against fitting of a single peak (bottom). Sticks representing the relative intensity and mean lattice parameter of each model are shown. (b) Weight fraction (top), lattice parameter (mid) and ratio (bottom) of the three structural models used to fit the inverse spinel peaks in the TTM reduction experiment.

parameters but common peak shape parameters (*i.e.* crystallite size and strain parameters). These peaks represent three populations of inverse spinel crystallites in the sample: ( $P_1$ ) raw TTM, ( $P_2$ ) an intermediate Ti enriched population, and ( $P_3$ ) Ti enriched crystallites at the highest Ti content.

The inclusion of three such sub-peaks was sufficient to fit the inverse spinel peaks. The inclusion of additional phases did not statistically improve the fit, whilst using only two phases yielded poor agreement with the experimental data. The lattice parameters fitted for each structural model were stable throughout the reduction (Fig. 7b), and the peak shape parameters were fixed.

Fig. 7b shows that during the reduction, the three sub-peak populations show fundamentally different behaviours. The initially dominant phase with the lowest Ti content, sub-peak  $P_1$ , is the only population to decrease in intensity during Stages II and III. This decrease continues until its intensity decreases to a similar magnitude as the other inverse spinel phases.

The detailed progression of each reduction stage is presented in further detail in the following sections.

**3.2.3. Stage 0: pre-reduction.** Prior to  $\text{H}_2$  reaching the sample ( $t < 0$ ), the measured wt% of crystallographic phases remains constant for both MAG and TTM. No solute

partitioning between phases occurs, shown by stability of peak position, shape and size for both hematite and inverse spinel.

**3.2.4. Stage I: hematite reduction.** Reduction of hematite to inverse spinel is the first phase transformation observed. This reaction proceeds rapidly and to effective completion for both TTM ( $t_1 = 1.4$  min) and MAG ( $t_1 = 2.1$  min) before any reduction of the inverse spinel occurs. This contrasts with the simultaneous progression observed in fluidised bed sampling of TTM (Fig. 3) in this and prior studies.<sup>16</sup>

In MAG, the direct reduction of hematite to magnetite occurs with no significant changes in peak shape or position (Fig. 8a).

For TTM, an increase in the titanohematite lattice parameter is observed during Stage I ( $t_0$  to  $t_1$ ). The inverse spinel unit cell simultaneously expands by 0.3% (Fig. 6b). This correlates with an increased Ti content in the phase as titanohematite reduces, producing the  $P_2$  and  $P_3$  crystallite populations (see Fig. 7b). Significant asymmetry of the diffraction peaks for inverse spinel in TTM occurs as a result (Fig. 8a). An increase in the low-angle side of the diffraction peaks (*i.e.*, larger unit cell) is particularly prominent. In addition, the fitted strain parameter of the inverse spinel phase shows a rapid increase by 40% during the hematite reduction.<sup>46</sup>



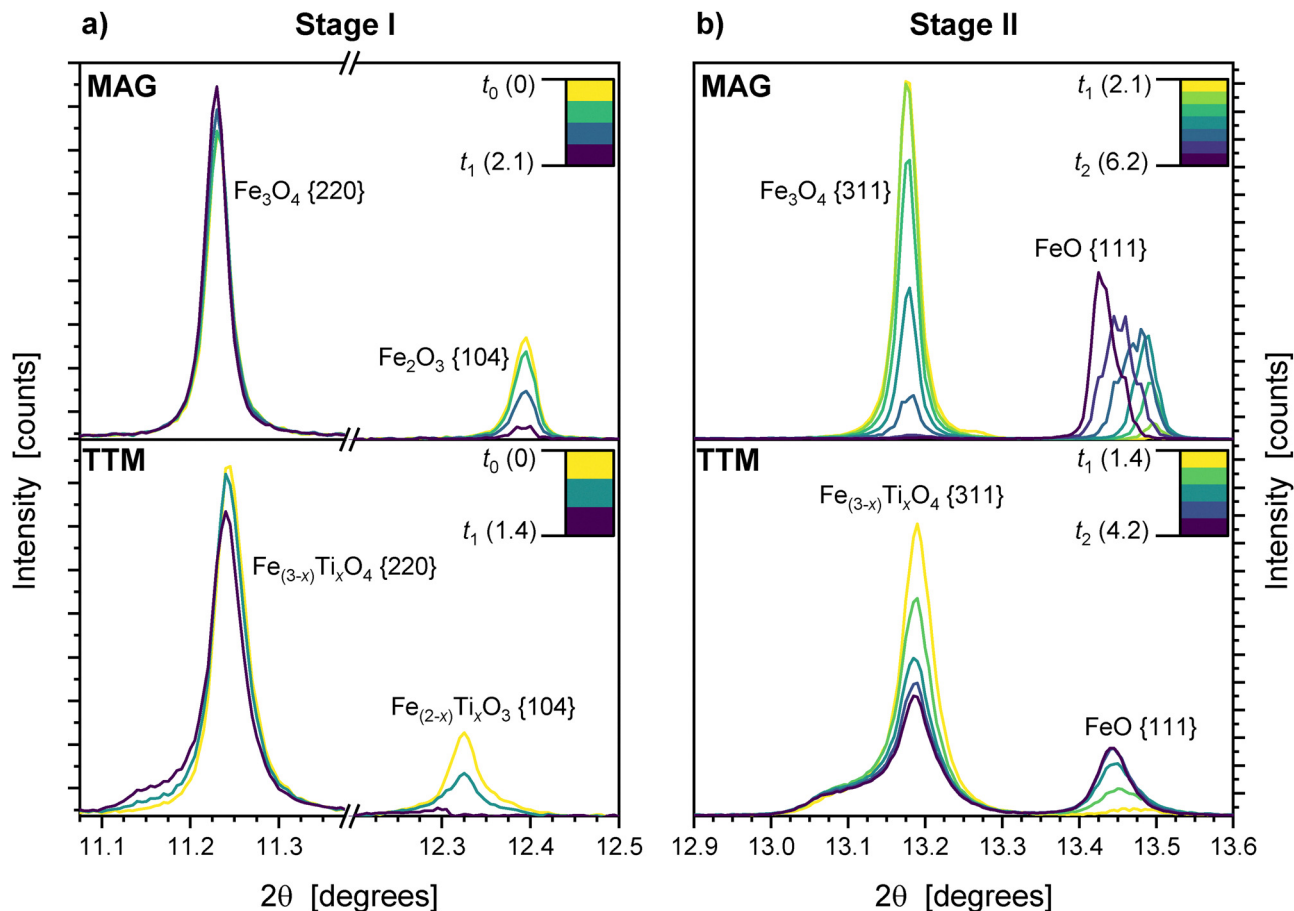


Fig. 8 Selected inverse spinel ( $\text{Fe}_{(3-x)}\text{Ti}_x\text{O}_4$ ), titanohematite ( $\text{Fe}_{(2-x)}\text{Ti}_x\text{O}_3$ ), and wüstite ( $\text{FeO}$ ) peaks during (a) Stage I conversion of hematite to inverse spinel reduction step and (b) Stage II conversion of inverse spinel to wüstite during synchrotron reduction experiments for samples of MAG (top) and TTM (bottom). The time in minutes from  $\text{H}_2$  switchover is indicated in the legends.

**3.2.5. Stage II: wüstite ( $\text{Fe}_{(1-x)}\text{O}$ ) formation.** The reduction of inverse spinel to wüstite characterises Stage II. In both MAG and TTM, increasing Fe:O ratio is shown by the increasing lattice parameter as reduction progresses (Fig. 8b). Wüstite is sub-stoichiometric with composition dependent on local oxygen fugacity, with increasing lattice parameter associated with an Fe:O ratio increasing towards 1.<sup>47,48</sup> This indicates that the first wüstite formed has a high oxygen content, with the average iron content increasing as the samples reduce.

Production of wüstite is the only reaction pathway in MAG during stage II (eqn (2)), reaching completion 4 minutes after the start of Stage II (Fig. 6a), with no  $\text{Fe}_3\text{O}_4$  present after this point ( $t_2 = 6.2$  min). The apparent rate of reduction slows at the end of Stage II, correlating with the increased stability and widening of the wüstite phase field at elevated temperature allowing stoichiometric deviation not captured in the estimated reduction degree.<sup>49</sup> There is no change in inverse spinel unit cell volume throughout this stage.

Total conversion to wüstite does not occur in TTM, with 59 wt% inverse spinel remaining at the peak wüstite concentration of 34 wt% ( $t_2 = 4.2$  min). Simultaneous reduction of wüstite is indicated by the formation of face-centred cubic

austenite ( $\gamma\text{-Fe}$ ), which increases in rate as the stage progresses and the reduction of  $\text{Fe}_{(3-x)}\text{Ti}_x\text{O}_4$  slows.

Increasing net concentration of Ti in the inverse spinel lattice is shown by a 0.3% expansion in the net unit cell volume (Fig. 6b). This is caused by reduction of low-Ti content crystallites, as represented by sub-peak  $\text{P}_1$  (Fig. 7b), and is visible as a decrease in the high-angle sub-peak of the inverse spinel diffraction peaks (Fig. 8b). No reduction of  $\text{P}_2$  or  $\text{P}_3$  occurs during this stage.

**3.2.6. Stage III: wüstite ( $\text{Fe}_{(1-x)}\text{O}$ ) reduction.** The reduction of wüstite to metallic iron occurs in both MAG and TTM in Stage III, with both austenite and body-centred cubic ferrite ( $\alpha\text{-Fe}$ ) present (Fig. 9a). At the end of Stage III, MAG achieves complete metallisation and undergoes no further reduction stages.

Wüstite in MAG is directly reduced to iron during Stage III, forming austenite and ferrite. This reaches completion after 25 minutes. No additional phases are formed during this process.

Metallic iron product phases had stable lattice parameters and peak shapes throughout.

The majority of wüstite present in TTM is reduced to iron during Stage III. The wüstite unit cell size continues to increase,



reaching a stable maximum of 4.365 Å. The reduction of inverse spinel also continues during Stage III at a decreased rate, with the continued reduction of the  $P_1$  sub-population. No accumulation of Ti occurs, shown by a plateau in unit cell size and the absence of  $P_2$  or  $P_3$  crystallite generation (Fig. 7b). This behaviour is the continued production of wüstite as channels coarsen at the core of the reducing particles.

At a reduction degree of approximately 60%, a change in the reduction mode of inverse spinel is observed. The reduction of  $P_1$  crystallites increases, with the generation of additional  $P_2$  crystallites. This indicates the direct reduction of inverse spinel, with the accumulation of Ti increasing the lattice parameter of the remaining inverse spinel. No new intermediate or Ti bearing phases are observed during this stage.

This correlates well with the intermediate regime established in fluidised bed reduction by Prabowo *et al.* between 850 and 950 °C,<sup>16</sup> above which the reduction of  $\text{Fe}_{(3-x)}\text{Ti}_x\text{O}_4$  halts, and below which no intermediate wüstite is formed.

**3.2.7. Stage IV: ilmenite ( $\text{FeTiO}_3$ ) formation.** Inverse spinel is reduced to ilmenite ( $\text{FeTiO}_3$ ) in TTM during Stage IV. This phase is clearly distinguished from the Ti enriched

titanohematite observed at  $t_0$ , with a 2.2% larger unit cell volume. The highest Ti content crystallites,  $P_3$ , reduce during this stage, with  $P_2$  becoming the primary crystallite population.

The unit cell volume of the ilmenite phase reduces by 0.3% throughout Stage IV, indicating a change in stoichiometry as more ilmenite is formed. Ilmenite peaks are symmetric throughout this stage. The crystallisation of a magnesium aluminate spinel phase, labelled as  $\text{MgAl}_2\text{O}_4$ , also occurs during Stage IV (Fig. 9b).

**3.2.8. Stage V: ilmenite ( $\text{FeTiO}_3$ ) reduction/rutile ( $\text{TiO}_2$ ) formation.** Ilmenite is reduced to rutile during Stage V (Fig. 9c). No other  $\text{TiO}_2$  polymorphs (*e.g.*, anatase) are detected. The magnesium aluminate spinel phase remains stable during Stage V, with no change in concentration, lattice parameter, or peak shape.

The rutile content increases as Stage V progresses towards completion, with 2.9 wt% present at the final reduction degree of 91% after 75 minutes. No significant changes in lattice parameters for  $\text{TiO}_2$  are observed. The lattice cell volume of ilmenite continues to decrease as observed in Stage IV, indicating further changes in composition, with the resulting diffraction peaks shifting to higher angle.

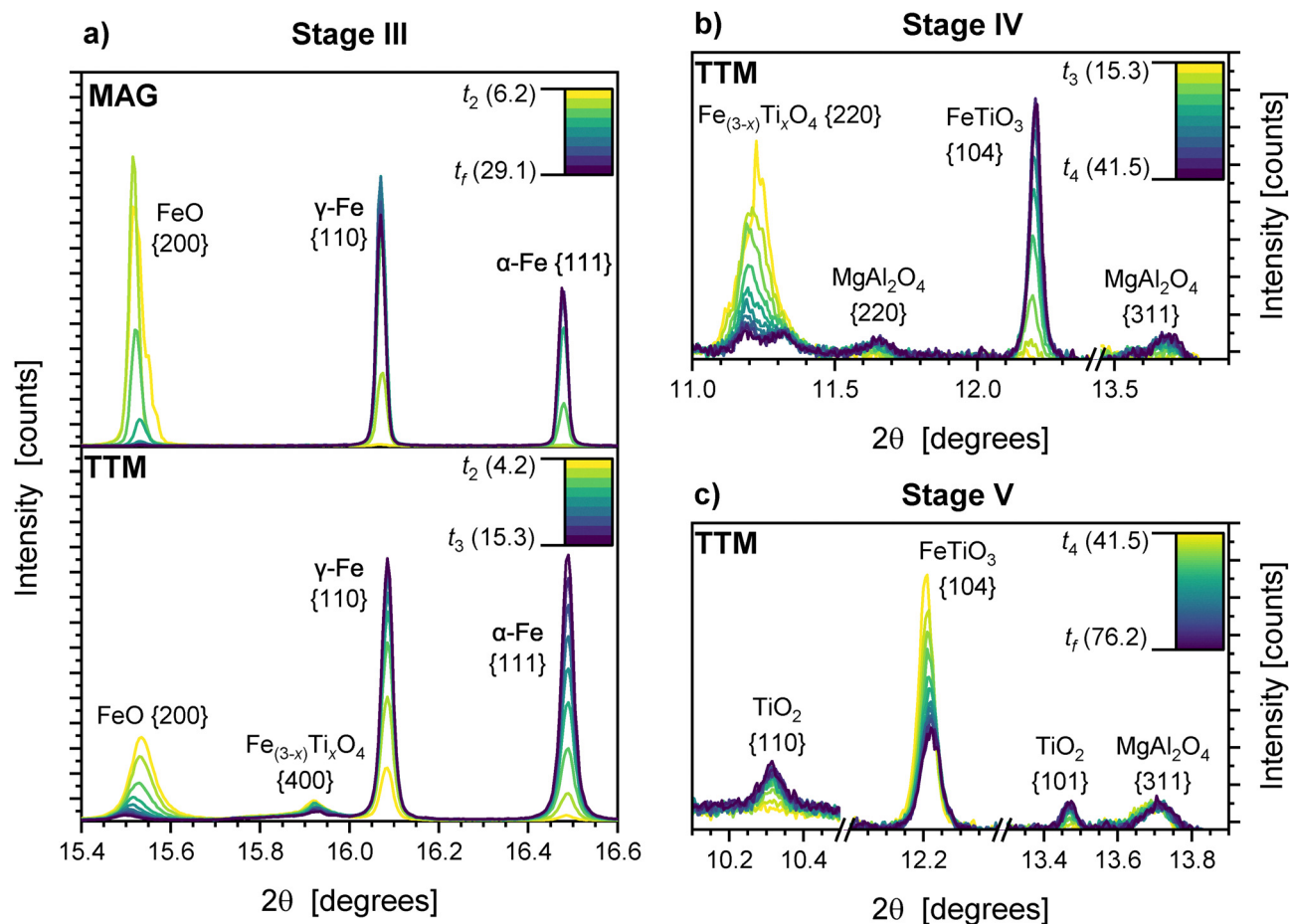


Fig. 9 Selected region of diffraction patterns showing the change in shape and position of peaks during isothermal reduction. The time in minutes from  $\text{H}_2$  switchover is indicated in the legends. (a) Wüstite ( $\text{FeO}$ ) and iron peaks during Stage III, for isothermal experiments on MAG (top) and TTM (bottom) samples. (b) Inverse spinel, spinel, and ilmenite peaks during Stage IV in TTM. (c) Rutile, spinel, and ilmenite peaks during Stage V in TTM.



## 4. Discussion

Combining measurement *in situ* with faster data sampling and increased angular resolution, the synchrotron diffraction results reveal significant new details of Ti migration during the reduction of TTM. Previous studies have lacked the time-resolution to observe the reduction of Ti enriched  $\text{Fe}_{(2-x)}\text{Ti}_x\text{O}_3$  during Stage I.<sup>16,17,27</sup> In this work, a significant change in the lattice parameter of inverse spinel is caused by this reduction (a). This is directly correlated with an increased and non-uniform Ti content in the inverse spinel matrix that forms the bulk of TTM particles. This contrasts with the MAG reference sample, where the reduction of hematite has no significant effect on the inverse spinel lattice parameter. No significant changes in the inverse spinel lattice parameter will be caused by oxygen content at this temperature, as the phase field remains narrow and approximately stoichiometric.

The higher solubility of Ti in the hematite-ilmenite solid solution compared to the magnetite-ulvospinel solution under equal oxygen partial pressures results in a higher total Ti content.<sup>50</sup> Titanohematite is not uniformly distributed in TTM, with approx. 8% of particles showing a lamellar microstructure consisting of inverse spinel and titanium enriched titanohematite, visible in the BSE micrographs shown in Supplementary C.<sup>17,51</sup> The Stage I reduction of hematite therefore produces a locally enriched inverse spinel, represented by

sub-peak  $P_3$  (Fig. 7). Resulting in a larger unit cell and a multimodal distribution of lattice parameter within the sample. A schema presenting the changes in sub-peaks and the attributed causes is presented below (Fig. 10).

From the changing ratio of sub-peaks during reduction, we posit that a Ti rich oxide is exsolved from the inverse spinel phase as it reduces. During Stage II, the net lattice parameter of the inverse spinel increases. This is caused predominantly by reduction of low Ti crystallites, represented by sub-peak  $P_1$  (Fig. 7b and 8b). There is no concurrent increase in sub-peaks  $P_2$  or  $P_3$ . The Ti contained in the reducing inverse spinel is therefore not retained in the remaining inverse spinel as posited in previous works.<sup>16,17</sup>

The crystalline product phase in Stage II is wüstite. Ti exhibits poor solubility in wüstite compared to the inverse spinel phase (Fig. 5a). Experimental reports indicate a solubility limit around 5at% at the liquidus of 1314 °C, with more recent thermodynamic analyses suggesting a maximum of <1 at% at 938 °C.<sup>52–54</sup> Tetravalent titanium must therefore be partitioned away from wüstite as reduction proceeds.

Given that no other crystalline phases are produced, this is direct evidence for the formation of an amorphous Ti rich oxide ( $a\text{-TiO}_n$ ) phase starting in Stage II. This correlates with the Ti-rich oxide shell formation observed in fluidised bed samples, that precipitates during Stage II and thickens throughout

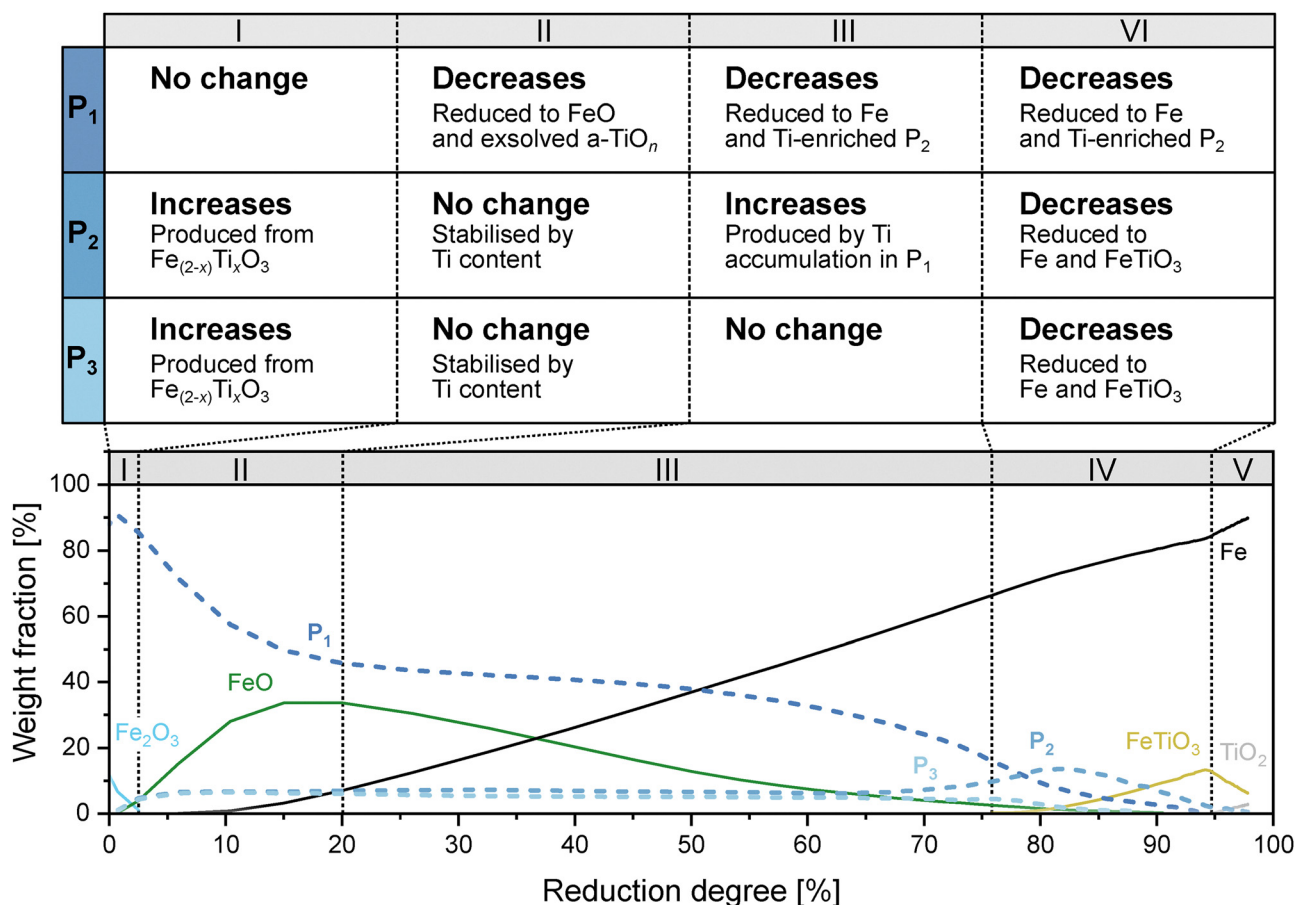
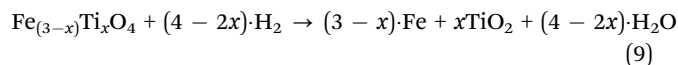


Fig. 10 Schema summarising the changes in the inverse spinel crystallite sub-populations during each reaction stage, and the causes of each change.

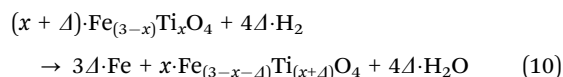


reduction (Fig. 5 and Supplementary C). The thickening of the shell correlates with wüstite formation, with the coarsening of wüstite channels at the core of the particle and the thickening of the shell terminating mid Stage III (Supplementary C). This behaviour disagrees with the theoretical reaction described in eqn (5), and can instead be better approximated as below:



This hypothesis is validated by considering the required diffusion of Ti in the inverse spinel phase to form the shell. Based on the 5  $\mu\text{m}$  thick reacted layer of wüstite channels at  $t = 60$  s, the estimated diffusion constant in inverse spinel is  $D_{\text{Ti}} \approx 10^{-13} \text{ m}^2 \text{ s}^{-1}$ . This lies well within the predicted diffusion rate of Fe in spinel structures at 950  $^\circ\text{C}$  and estimated oxygen partial pressure of  $p_{\text{O}_2} = 10^{-16}$  ( $p_{\text{H}_2\text{O}} = 0.3 \text{ atm}$ ).<sup>55</sup> Accurate data for the diffusion rate of Ti in inverse spinel is, however, limited to temperatures above 1100  $^\circ\text{C}$  and oxygen fugacity above  $10^{-11}$ .<sup>56</sup> This comparison neglects accelerated diffusion of grain boundaries and high vacancy content during reduction, which would further encourage the likely shell-exsolution mechanism.

A significant transition in reduction mechanism occurs in Stage III. As the available wüstite approaches zero, the reduction of remaining  $P_1$  crystallites accelerates. An increase in  $P_2$  crystallites indicates a transition in reaction pathway, with Ti being accumulated rather than primarily exsolved. This represents the direct reduction of inverse spinel to metallic iron, described by eqn (10):



A temperature dependent transition in the reduction of magnetite directly to Fe is well established, occurring below 570  $^\circ\text{C}$ .<sup>57</sup> The stabilising effect of Ti plays a similar role, lowering the favourability of the wüstite reduction route. The continued reduction of the inverse spinel during Stage III is visible as increasing metallisation within regions where wüstite reduction is already complete (Fig. 5b and Supplementary C).

The final key transition in behaviour is the direct conversion of inverse spinel to ilmenite in Stage IV. Each of these reduction pathways – described here as exsolution, accumulation, and conversion – demonstrate the preferential reduction of low-Ti content inverse spinel  $\text{Fe}_{(3-x)}\text{Ti}_x\text{O}_4$ , *i.e.*, the stabilisation of the phase by Ti. It is exclusively the low Ti  $P_1$  crystallites that are reduced throughout Stages II–III (Fig. 10), with the  $P_2$  crystallites dominant at the end of reduction.

Whilst there is an inhomogeneous distribution of inverse spinel across these three populations, considered as a collective body, the crystalline system follows the anticipated phase diagram well. An approximate ternary phase diagram for the Fe–Fe<sub>2</sub>O<sub>3</sub>–TiO<sub>2</sub> system at 950  $^\circ\text{C}$  is presented in Fig. 11a.<sup>49,50,58–60</sup> Of note is the instability of pseudobrookite ( $\text{FeTi}_2\text{O}_5$ ), with the limit of stability for the  $\text{M}_3\text{O}_5$  solid solution lying at approximately  $\text{Fe}_{1.3}\text{Ti}_{1.7}\text{O}_5$ .<sup>24</sup>

Cross-referencing the reduction stages described for TTM with the equilibrium phase assemblages A–J results in the following:

- (1) Stage I: conversion of titanohematite to a fully inverse spinel sample (A).
- (2) Stage II: net Ti content in inverse spinel increases as wüstite is formed (B).
- (3) Stage III: transition to the reduction of wüstite to metallic Fe, with no change in the Ti content of inverse spinel during

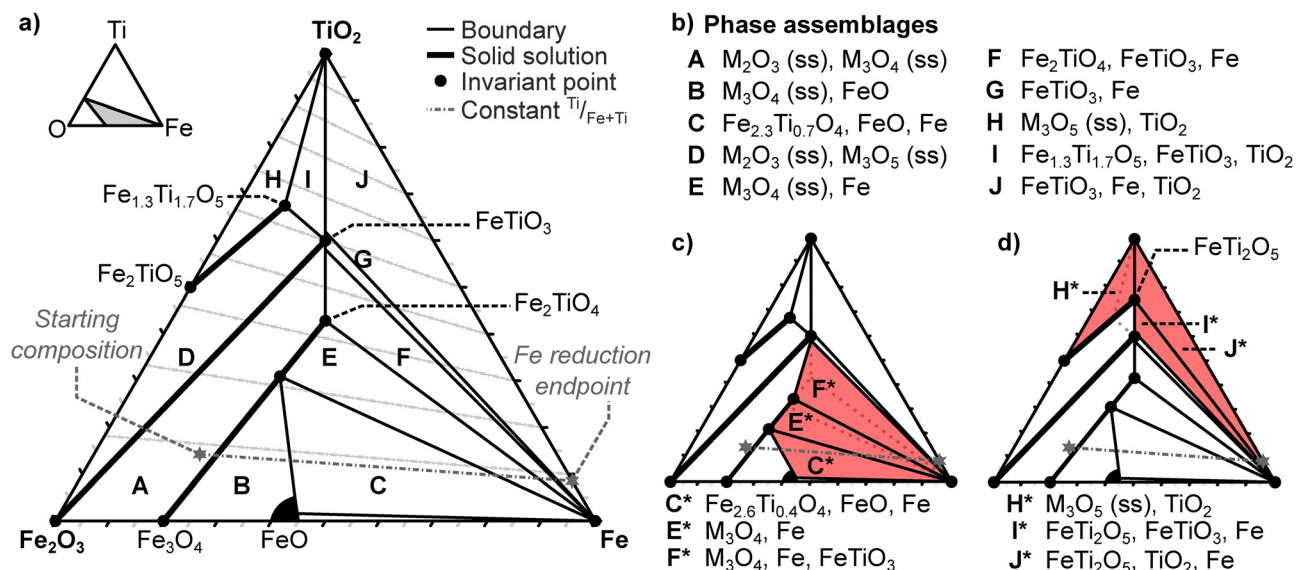


**Fig. 11** (a) Schematic molar fraction ternary Fe–Fe<sub>2</sub>O<sub>3</sub>–TiO<sub>2</sub> phase diagram for 950  $^\circ\text{C}$ , with the inclusion of established ferro-pseudobrookite stability limit at  $\text{Fe}_{1.3}\text{Ti}_{1.7}\text{O}_5$ .<sup>24,49,50,58–60</sup> The theoretical reduction pathway for titanomagnetite with a Ti/(Ti + Fe) ratio of 8.6% is shown. (b) Summary of phase assemblages A–J for the ternary diagram, where M represents metal cation; (ss) = solid solution. (c) Conceptual ternary phase diagram overlaid with the phase assemblages C\*–F\* for lower Ti content invariant points in inverse spinel. (d) Phase fields H\*–J\* if pseudobrookite is stabilised.



this period (C). At the end of Stage III, see the direct reduction of inverse spinel, resulting in an increasing lattice parameter (E).

(4) Stage IV: remaining inverse spinel is converted to ilmenite and metallic Fe (F and G).

(5) Stage V: ilmenite is converted to rutile and metallic Fe (J).

Minor deviations can be considered in terms of the position of specific vertices. Given that the net Ti content of inverse spinel never reaches that of  $P_3$ , it is clear that the ulvospinel point is never reached. Combined with the transition to Stage III, a conceptual modification is shown in Fig. 11c. Instability of the ulvospinel has previously been reported, no longer co-occurring with metallic Fe below 680 °C.<sup>50</sup> It is important to note that this neglects the exsolved Ti rich amorphous oxide, which is not observed in previous reports of the Fe–Ti–O ternary at 950 °C and is incompatible with the thermodynamic predictions of the equilibrium ternary.<sup>58,61</sup>

This ternary phase diagram is also broadly consistent with the reported behaviour of high Ti titanomagnetite ores. At a Ti/(Ti + Fe) ratio of 22%, material sourced from Chaoyang is reported to partially metallise before directly reducing to ilmenite (transiting phase assemblages A–E–F–G), with no wüstite formation reported.<sup>15</sup> This contrasting behaviour emphasises the significance of the Ti concentration in the TTM source material in determining the reduction pathway for titanomagnetites.

The formation of pseudobrookite or rutile during Stage V is the only significant difference between fluidised bed and synchrotron reduction experiments. The Ti rich end-member of  $Fe_{(2-x)}Ti_{(1+x)}O_5$  is typically unstable below 1150 °C, and less stable than rutile at high oxygen fugacity.<sup>24,50</sup> Magnesium cations are the likely cause of pseudobrookite formation as a stabiliser of  $M_3O_5$  phases.<sup>62</sup> The observed pseudobrookite has a high Mg content, shown by a contracted  $c$  axis and elongated  $b$  axis ( $a = 9.742$  Å,  $b = 10.09$  Å,  $c = 3.738$  Å).<sup>42,63</sup> As shown schematically in Fig. 11d, stabilisation of a pseudobrookite phase will encourage its formation at high reduction degrees. Considering the migration of Mg to the shell (Fig. 5b and Supplementary C), the smaller particle size and difference in gas flow behaviour between experiments may play a role in this variation.

Magnesium cations also play a role in the formation of a spinel phase during Stage IV. A shift in lattice parameter compared to the titanomagnetite inverse spinel (8.18 Å vs. 8.54 Å) correlates well with a primarily magnesium aluminate spinel, with low Ti or Fe content.<sup>64,65</sup> This phase however is present in low concentrations and only apparent during Stage IV–V. The remaining Al and Mg cations must instead be substituting for Fe or Ti in the inverse spinel or ilmenite lattices or exsolving as amorphous oxides during Stages I–III.

This same cationic substitution prevents direct extrapolation of Ti content from lattice parameters, and may explain the anomalously low inverse spinel unit cell size in TTM compared to MAG. Al and Mg account for 5.1 and 4.8 at% of cations respectively (Table 1). Microstructural analyses indicate co-location of Ti and Al during reduction (Section 3.1.2. and Supplementary C), both of which preferentially occupy the octahedral lattice site in the inverse spinel phase.<sup>66–68</sup> Titanium in particular is well-established to occupy the octahedral

vacancy site, even at high Ti:Fe ratios approaching the ulvospinel composition.<sup>69</sup> The combination of their impact on lattice expansion is, however, unlikely to be linear given the significance of cation ordering in determining lattice parameters.<sup>38,70</sup> Local oxygen fugacity, interstitial hydrogen and the established discontinuity in thermal expansion above the Curie temperature will further confound lattice expansion.<sup>38,39,71</sup> This provides a likely explanation for the lower initial lattice parameter observed in TTM than MAG at temperature, despite the anticipated lattice expansion caused by Ti.

Similar confounding effects may be anticipated in ilmenite. Oxygen vacancies, interstitial hydrogen, decreasing Ti or increasing Al content would all contribute to an observed decrease in lattice parameter.<sup>20,31,72</sup> This further reinforces the challenges of accurately measuring the movement of a single solute species in mineral systems, where the migration of other solutes present alters lattice parameters. Further work with high purity synthetic titanomagnetite and magnetite would be needed to decouple these effects.

Given the established  $\gamma$ – $\alpha$  transition temperature of 912 °C in pure Fe, the presence of ferrite in both MAG and TTM at 938 °C is unexpected, and can only be explained as a compositional effect. First, the low illuminated volume ( $>0.4$  mm<sup>3</sup>) eliminates the possibility of a large thermal gradient across the sample. Second, the  $\alpha$ : $\gamma$  ratio increases in both MAG and TTM with time, ruling out local endothermic cooling during the rapid early reaction, which would favour early ferrite formation. Finally, *in situ* platinum wire calibration indicates a constant temperature within the hot zone during the experiment, ruling out a thermal drift of the whole system. There remains considerable ferrite present at the endpoint for both MAG and TTM at 938 °C. Nitridation by nitrogen carrier gas has been observed *via* synchrotron to widen the  $\gamma$ – $\alpha$  transition temperature,<sup>73</sup> but the use of pure hydrogen in this work excludes this factor. Both samples contain several strongly  $\alpha$ -stabilising elements (Ti, Al, V, Si), with approximately 0.4 at% Ti in solution sufficient to completely eliminate austenite at 938 °C.<sup>49</sup> None of these elements are directly reducible to a metallic state from their oxides under the reaction conditions investigated in this work. However, the presence of a large sink of metallic Fe will alter the activity of these elements.

Calculation of the equilibrium phase distribution and activities of elements in each phase (FactSage v8.2, FactPS/FactOxid/FactStel) does not indicate body-centred cubic ferrite as a stable end-phase for either MAG or TTM (Supplementary F). Austenite and spinel phases are indicated as the predominant stable phases. The microstructural partitioning of solutes during the reduction process clearly plays a key role in determining the stable end phases present.

This work demonstrates the significant effect of Ti on direct reduction behaviour of titanomagnetite ore. The exsolution of amorphous oxides has an established effect on particle sticking during fluidised bed reduction,<sup>16,17</sup> and will influence downstream processing of reduced material. Further study is required to confirm the mechanistic cause of this exsolution behaviour, and the role of other cation substituents in the inverse spinel matrix.



## Conclusions

In this study, *in situ* synchrotron X-ray diffraction was used to analyse the hydrogen reduction of New Zealand titanomagnetite ironsand at 938 °C, to better characterise the fluidised bed reduction behaviour. The importance of Ti content in determining the reduction pathway was confirmed. The key findings are:

(1) The behaviour observed *in situ* is representative of fluidised bed reduction behaviour, with only minor deviations in reduction pathway at the end stage of reduction.

(2) A 5-stage reduction pathway is observed compared to the typical 3-stage pathway of a synthetic magnetite sample.

(3) The presence of titanium enriched titanohematite leads to a trimodal Ti content in the inverse spinel phase and asymmetric diffraction peaks during reduction.

(4) Ti stabilises the inverse spinel phase, preventing total reduction *via* wüstite at this temperature, and favouring the reduction of low Ti content crystallites first.

(5) Titanium is exsolved from the inverse spinel during reduction to wüstite, resulting in an amorphous Ti rich oxide shell.

(6) A transition to direct reduction of inverse spinel occurs late in Stage III, resulting in the accumulation of Ti in the remaining inverse spinel.

## Author contributions

The contributions of the authors to the current work are as follows: conceptualization: B. I., M. J. R., S. P., M. N., M. H. R. and C. W. B.; data curation: M. L., B. I., B. M., S. S. and M. H. R.; formal analysis: M. L., B. I. and R. J. L.; funding acquisition: R. J. L., B. J. M., M. H. R. and C. W. B.; investigation: B. I., M. J. R., B. M., S. S. and M. H. R.; methodology: B. I., M. J. R., B. M. and M. H. R.; supervision: B. J. M., M. H. R. and C. W. B.; visualization: M. L.; writing – original draft: M. L. and B. I.; writing – review and editing: M. L., S. P., M. N., R. J. L., B. J. M. and C. W. B.

## Conflicts of interest

There are no conflicts to declare.

## Data availability

Data for this article are available at <https://doi.org/10.17605/OSF.IO/WQT58>. This includes data collected from the ANSTO synchrotron diffraction facility including raw and intensity corrected files.

Supplementary information (SI): (A) photographs of experimental apparatus; (B) parameters for TOPAS fitting; (C) SEM and EDS maps of fluidised bed reduced particles; (D) reported data for compositional and thermal dependence of lattice parameters; (E) comparison of *in situ* synchrotron and fluidised bed XRD; (F) calculation of theoretical equilibrium phases. See DOI: <https://doi.org/10.1039/d5ma01165e>.

## Acknowledgements

This research was undertaken on the Powder Diffraction beamline at the Australian Synchrotron, part of ANSTO [reference number AS171/PD/11627]. This work was supported by New Zealand Ministry of Business, Innovation and Employment [grant numbers RTVU1404 and RTVU1907]. Martin J. Ryan is acknowledged posthumously as a significant contributor to this work.

## References

- 1 J. Kim, B. K. Sovacool, M. Bazilian, S. Griffiths, J. Lee, M. Yang and J. Lee, *Energy Res. Soc. Sci.*, 2022, **89**, 102565.
- 2 International Energy Agency, *Emissions Measurement and Data Collection for a Net Zero Steel Industry*, OECD, Paris, 2023.
- 3 W. Choi and S. Kang, *J. Environ. Manage.*, 2023, **335**, 117569.
- 4 M. Sun, K. Pang, M. Barati and X. Meng, *J. Sustainable Metallurgy*, 2024, **10**, 10–25.
- 5 R. J. Holmes, Y. Lu and L. Lu, *Iron Ore*, Elsevier, 2022, pp. 1–56.
- 6 J. H. Luo, K. H. Qiu, Y. C. Qiu and P. C. Zhang, *Adv. Mater. Res.*, 2013, **813**, 292–297.
- 7 L. M. L. Harahap, A. Idrus, Ernowo, I. G. Sukadana, Suwahyudi and T. Handayani, *IOP Conf. Ser.: Earth Environ. Sci.*, 2023, **1233**, 012022.
- 8 S. Samanta, M. C. Goswami, T. K. Baidya, S. Mukherjee and R. Dey, *Int. J. Miner., Metall. Mater.*, 2013, **20**, 917–924.
- 9 R. L. Brathwaite, M. F. Gazley and A. B. Christie, *J. Geochem. Explor.*, 2017, **178**, 23–34.
- 10 Z. Yan, S. Zheng, Y. Zhang and Y. Zhang, *JOM*, 2025, **77**, 3354–3367.
- 11 A. Orpin, H. Bostock, S. Nodder, P. Barnes and G. Lamarche, *Coasts and Ports 2009: In a Dynamic Environment*, 2009, pp. 90–96, DOI: [10.3316/INFORMIT.866385506331874](https://doi.org/10.3316/INFORMIT.866385506331874).
- 12 R. L. Brathwaite, A. B. Christie and M. F. Gazley, *Miner. Depos.*, 2021, **56**, 343–362.
- 13 C. van Vuuren, A. Zhang, J. T. Hinkley, C. W. Bumby and M. J. Watson, *Cleaner Chem. Eng.*, 2022, **4**, 100075.
- 14 M. Girdwood, A. C. Percy, T. Arif, K. Dahm, A. T. Marshall and C. W. Bumby, *ACS Sustainable Chem. Eng.*, 2025, **13**, 4376–4385.
- 15 J. Yu, N. Hu, H. Xiao, P. Gao and Y. Sun, *Powder Technol.*, 2021, **385**, 83–91.
- 16 S. W. Prabowo, R. J. Longbottom, B. J. Monaghan, D. del Puerto, M. J. Ryan and C. W. Bumby, *Powder Technol.*, 2022, **398**, 117032.
- 17 S. W. Prabowo, R. J. Longbottom, B. J. Monaghan, D. del Puerto, M. J. Ryan and C. W. Bumby, *Metall. Mater. Trans. B*, 2019, **50**, 1729–1744.
- 18 F. J. Berry, C. Greaves, Ö. Helgason, J. McManus, H. M. Palmer and R. T. Williams, *J. Solid State Chem.*, 2000, **151**, 157–162.
- 19 C. Melai, T. Boffa Ballaran, L. Uenver-Thiele, A. Kurnosov, A. I. Chumakov, D. Bessas and D. J. Frost, *Phys. Chem. Miner.*, 2023, **50**, DOI: [10.1007/s00269-022-01217-2](https://doi.org/10.1007/s00269-022-01217-2).
- 20 J. Majzlan, A. Navrotsky and B. J. Evans, *Phys. Chem. Miner.*, 2002, **29**, 515–526.



- 21 Y. Kapelyushin, Y. Sasaki, J. Zhang, S. Jeong and O. Ostrovski, *Metall. Mater. Trans. B*, 2015, **46**, 2564–2572.
- 22 Z. Wang, J. Zhang, Z. Liu, K. Jiao and X. Xing, *JOM*, 2019, **71**, 1776–1784.
- 23 J. Yu, Y. Ou, Y. Sun, Y. Li and Y. Han, *Powder Technol.*, 2022, **402**, 117340.
- 24 I. E. Grey and R. R. Merritt, *J. Solid State Chem.*, 1981, **37**, 284–293.
- 25 K. I. Lilova, C. I. Pearce, C. Gorski, K. M. Rosso and A. Navrotsky, *Am. Mineral.*, 2012, **97**, 1330–1338.
- 26 R. J. Harrison, U. Becker and S. A. T. Redfern, *Am. Mineral.*, 2000, **85**, 1694–1705.
- 27 S. W. Prabowo, R. J. Longbottom, B. J. Monaghan, D. del Puerto, M. J. Ryan and C. W. Bumby, *JOM*, 2022, **74**, 885–898.
- 28 V. Materić, B. Ingham and R. Holt, *CrystEngComm*, 2015, **17**, 7306–7315.
- 29 S. K. Kuila, R. Chatterjee and D. Ghosh, *Int. J. Hydrogen Energy*, 2016, **41**, 9256–9266.
- 30 A. Heidari, M. K. Ghosalya, M. Alaoui Mansouri, A. Heikkilä, M. Iljana, E. Kokkonen, M. Huttula, T. Fabritius and S. Urpelainen, *Int. J. Hydrogen Energy*, 2024, **83**, 148–161.
- 31 N. E. Brown, A. Navrotsky, G. L. Nord and S. K. Banerjee, *Am. Mineral.*, 1993, **78**, 941–951.
- 32 P. Fabrykiewicz, M. Stękiel, I. Sosnowska and R. Przeniosło, *Acta Crystallogr., B: Struct. Sci. Cryst. Eng. Mater.*, 2017, **73**, 27–32.
- 33 J. Song, D. Fan, S. Huang, S. Zhang, M. Wu, W. Chen and W. Zhou, *Acta Geochim.*, 2023, **42**, 988–997.
- 34 R. J. Harrison and S. A. T. Redfern, *Phys. Chem. Miner.*, 2001, **28**, 399–412.
- 35 B. A. Wechsler and C. T. Prewitt, *Am. Mineral.*, 1984, **69**, 176–185.
- 36 C. I. Pearce, C. M. B. Henderson, N. D. Telling, R. A. D. Patrick, J. M. Charnock, V. S. Coker, E. Arenholz, F. Tuna and G. van der Laan, *Am. Mineral.*, 2010, **95**, 425–439.
- 37 G. R. Holcomb, *Mater. High Temp.*, 2019, **36**, 232–239.
- 38 D. Levy, R. Giustetto and A. Hoser, *Phys. Chem. Miner.*, 2012, **39**, 169–176.
- 39 D. Levy, G. Artioli and M. Dapiaggi, *J. Solid State Chem.*, 2004, **177**, 1713–1716.
- 40 C. A. McCammon and L. Liu, *Phys. Chem. Miner.*, 1984, **10**, 106–113.
- 41 I. Seki and K. Nagata, *ISIJ Int.*, 2005, **45**, 1789–1794.
- 42 W. Q. Guo, S. Malus, D. H. Ryan and Z. Altounian, *J. Phys.: Condens. Matter*, 1999, **11**, 6337–6346.
- 43 D. Y. Chung, P. J. Heaney, J. E. Post, J. E. Stubbs and P. J. Eng, *J. Phys. Chem. Solids*, 2023, **177**, 111284.
- 44 Y. Hamano, *J. Geomagnet. Geoelectricity*, 1989, **41**, 65–75.
- 45 R. A. Fischer, A. J. Campbell, G. A. Shofner, O. T. Lord, P. Dera and V. B. Prakapenka, *Earth Planet. Sci. Lett.*, 2011, **304**, 496–502.
- 46 Y. Waseda, E. Matsubara and K. Shinoda, *X-Ray Diffraction Crystallography*, Springer Berlin Heidelberg, Berlin, Heidelberg, 2011, pp. 107–167.
- 47 R. M. Hazen and R. Jeanloz, *Rev. Geophys.*, 1984, **22**, 37–46.
- 48 M. Hamada, S. Ganschow, D. Klimm, G. Serghiou, H.-J. Reichmann and M. Bickermann, *Z. Naturforsch. B*, 2022, **77**, 463–468.
- 49 A. Walnsch, A. Leineweber and M. J. Kriegel, *Calphad*, 2023, **81**, 102555.
- 50 K. Borowiec and T. Rosenqvist, *Scand. J. Metall.*, 1981, **10**, 217–224.
- 51 E. Park and O. Ostrovski, *ISIJ Int.*, 2003, **43**, 1316–1325.
- 52 C. Gleitzer, *Diversity and complexity of the wustite solid solutions i-tentative rationalization of the miscibility data and classification of the wustite ternary fields and of the postsaturation reactions*, 1980, vol. 15.
- 53 J. B. MacChesney and A. Muan, *Am. Mineral.: J. Earth Planetary Mater.*, 1961, **46**, 572–582.
- 54 T. Jantzen, K. Hack, E. Yazhenskikh and M. Müller, *Calphad*, 2018, **62**, 187–200.
- 55 J. A. Van Orman and K. L. Crispin, *Rev. Mineral. Geochem.*, 2010, **72**, 757–825.
- 56 S. Aggarwal and R. Dieckmann, *Phys. Chem. Miner.*, 2002, **29**, 707–718.
- 57 P. Li, Y. Li, J. Yu, P. Gao and Y. Han, *Int. J. Hydrogen Energy*, 2022, **47**, 31140–31151.
- 58 S. K. Gupta, V. Rajakumar and P. Grieveson, *Canadian Metall. Quarterly*, 1989, **28**, 331–335.
- 59 P. Den Hoed and A. Luckos, *Oil Gas Sci. Technol.–Revue d'IFP Energies nouvelles*, 2011, **66**, 249–263.
- 60 N. Kumagai, T. Hiraki, U. B. Pal, E. Kasai and T. Nagasaka, *Metall. Mater. Trans. B*, 2018, **49**, 2278–2284.
- 61 N. Kumagai, T. Hiraki, U. B. Pal, E. Kasai and T. Nagasaka, *Metall. Mater. Trans. B*, 2018, **49**, 2278–2284.
- 62 O. M. Borysenko, S. M. Logvinkov, G. M. Shabanova and I. A. Ostapenko, *Voprosy Khimii i Khimicheskoi Tekhnologii*, 2021, 12–15.
- 63 D. Xirouchakis, A. Smirnov, K. Woody, D. H. Lindsley and D. J. Andersen, *Am. Mineral.*, 2002, **87**, 658–667.
- 64 S. A. T. Redfern, R. J. Harrison, H. S. C. O'Neill and D. R. R. Wood, *Am. Mineral.*, 1999, **84**, 299–310.
- 65 W. Sugimoto, N. Kaneko, Y. Sugahara and K. Kuroda, *J. Ceram. Soc. Jpn.*, 1997, **105**, 101–105.
- 66 F. Bosi, U. Halenius and H. Skogby, *Am. Mineral.*, 2009, **94**, 181–189.
- 67 A. V. Kovalevsky, E. N. Naumovich, A. A. Yaremchenko and J. R. Frade, *J. Eur. Ceram. Soc.*, 2012, **32**, 3255–3263.
- 68 A. V. Kovalevsky, A. A. Yaremchenko, E. N. Naumovich, N. M. Ferreira, S. M. Mikhalev, F. M. Costa and J. R. Frade, *J. Eur. Ceram. Soc.*, 2013, **33**, 2751–2760.
- 69 M. Okube, T. Oshiumi, T. Nagase, R. Miyawaki, A. Yoshiasa, S. Sasaki and K. Sugiyama, *J. Synchrotron Radiat.*, 2018, **25**, 1694–1702.
- 70 S. M. Antao, I. Hassan and J. B. Parise, *Am. Mineral.*, 2005, **90**, 219–228.
- 71 I. Kinebuchi and A. Kyono, *J. Mineral. Petrol. Sci.*, 2021, **116**, 211–219.
- 72 C. E. Cava, L. S. Roman and C. Persson, *Phys. Rev. B: Condens. Matter Mater. Phys.*, 2013, **88**, 045136.
- 73 Y. Wang, A. Heidari, H. Singh, G. King, S. Wang, R. F. Chuproski, M. Huttula, T. Fabritius and S. Urpelainen, *Metall. Mater. Trans. B*, 2025, **56**, 5759–5772.

